

# Enhanced Visible Light Response in Engineered Strontium Iodide Monolayer for Optoelectronic Applications

Received 1 November, 2024; revised 27 November, 2024; accepted 28 November, 2024

Vipin Kumar<sup>a,\*</sup>, Upendra Kumar<sup>b</sup>, Gyanendra Kumar Maurya<sup>c</sup>, Pushpendra Kumar<sup>d,\*</sup>, and Jin Seog Gwag<sup>a,\*</sup>

<sup>a</sup>Department of Physics, Yeungnam University, Gyeongsan 38541, Republic of Korea

<sup>b</sup>Scientific Computing Laboratory, Center for Study of Complex Systems, Institute of Physics Belgrade, University of Belgrade, Belgrade 11080, Serbia

<sup>c</sup>Department of Physics, GLA University, Mathura 281406, India

<sup>d</sup>Department of Physics, Manipal University Jaipur, Jaipur 303007, Rajasthan, India

\*Corresponding author E-mail: [pushpendra.kumar@jaipur.manipal.edu](mailto:pushpendra.kumar@jaipur.manipal.edu), [sweat3000@ynu.ac.kr](mailto:sweat3000@ynu.ac.kr)

## ABSTRACT

Atomically thin materials have attracted attention because of their unique physical properties. Several two-dimensional (2D) materials have been synthesized and screened experimentally and theoretically. Among these, alkaline earth metal-based 2D materials exhibit unique physical properties and have numerous applications in electronics, optoelectronics, dentistry, and scintillators. In this study, the single layer of strontium iodide, a 2D alkaline earth metal halide, was investigated for its structural, electronic, and optoelectronic properties using density functional theory, and a comparative analysis was performed with other similar materials. These investigations also covered frequency- and polarization-dependent dielectric and optical functions. Substitutional doping with lanthanide series elements (Nd, Sm, and Ho) was performed. The obtained results indicate the significant role of these dopants in tuning electronic and optical quantities. The increased static refractive index of the doped materials indicates enhanced reflection owing to the backscattering of the incident light from the impurity atoms. The optical conductivity is significantly improved in the visible region. Our findings suggest that these monolayer materials have potential applications in visible light, ultraviolet-C, and vacuum ultraviolet absorbers, anti-reflection coatings, and highly reflective systems. Hence, these materials are excellent candidates for nanoelectronic and optoelectronic devices.

**Keywords:** Two-dimensional materials, Electronic properties, Doping, Optoelectronic properties, Density functional theory

## 1. Introduction

Bulk alkaline earth metal dihalides exhibit  $\text{MX}_2$ -type chemical formulae. M (=Mg, Ca, Sr, and Ba) represents group IIA alkaline earth metals, and X (F, Cl, Br, and I) represents group VIIA halogen elements of the periodic table. These compounds exhibit interesting structural and electronic properties, ranging from insulating to semi-conducting behavior [1,2]. Fluoride-based group IIA compounds, such as magnesium fluoride ( $\text{MgF}_2$ ) [3] and calcium fluoride [4,5] are well known for their high melting points and transparency in the ultraviolet (UV) region, making them valuable for optical applications. Chloride, bromide, and iodide-based group IIA compounds [e.g., strontium chloride ( $\text{SrCl}_2$ ), barium bromide, and barium iodide ( $\text{BaI}_2$ )] tend to have larger ionic sizes and lower melting points than their fluoride counterparts [6]. Some exhibit excellent luminescence properties under specific conditions, which are particularly interesting for lighting and display technologies [7]. The varying ionic radii of alkaline earth metals and halogens significantly influence their lattice crystal structure [8], often forming orthorhombic or cubic phases. The bandgaps of group IIA-VIIA-based compounds generally range from wider [9,10] to narrower [11]. A few of them also show potential in different fields such as catalysis [12,13] and scintillation [14]. The M

cations and X anions in strontium iodide ( $\text{SrI}_2$ ) create stable hole polarons with intricate migration paths, enabling rapid carrier diffusion. This distinct interaction significantly enhances the scintillation performance of  $\text{SrI}_2$  [14]. Their applications span various fields, including optoelectronics, photonics, and catalysis, owing to their wide bandgap and high chemical stability [15].

$\text{SrI}_2$  is a member of the  $\text{MX}_2$ -type class of materials. This is similar to the IA-IIA heavy metal halides, which exhibit a wide bandgap under ambient conditions [16,17].  $\text{SrI}_2$  is used as a scintillator [14]. The Eu-doped  $\text{SrI}_2$  shows a short decay time (1.2  $\mu\text{s}$ ) and can achieve a high light yield (115,000 Photons/MeV) [18,19]. Its high atomic number and density provide  $\text{SrI}_2$  with excellent stopping power for irradiation. Despite these advantages, the use of  $\text{SrI}_2$  was limited for a long time after its discovery [20] until the successful growth of large single crystals [18]. However, the crystallization of this material with a distorted Pbc structure is intricate, making crystal growth difficult during the synthesis process. Significant efforts have been made to expand its applications by enhancing its physical properties via doping and codoping methods and advancing crystal growth techniques to reduce production costs and improve economic viability [21,22].

The reported bandgap of orthorhombic  $\text{SrI}_2$  is approximately 4.5 eV, characterized by a charge transfer between the iodine  $p$ -orbital



[contributing to the valence band (VB)] and the metal atom [contributing to the conduction band (CB)] [23]. This charge transfer underscores the distinct chemical nature of the two I sites (I1 and I2) in the orthorhombic  $\text{SrI}_2$  structure. This leads to a more favorable Coulomb potential for the I2 sites. This results in a lower density of states (DOS) for I2 than I1, reflecting the energy differences between these sites [23]. Eu-doped  $\text{SrCl}_2$  microcrystals embedded in a NaCl matrix exhibit unique properties, influenced by the temperature and concentration of Eu ions [24]. Hence, owing to their distinctive luminescence behavior, the  $\text{SrCl}_2$ -Eu microcrystals are excellent candidates for optoelectronic devices. Sm-doped  $\text{SrCl}_2$  crystals exhibit strong scintillation properties, highlighted by a broad emission band centered at 680 nm [25]. This emission is primarily attributed to the  $5d4f$  electronic transitions of  $\text{Sm}^{2+}$  ions, making this crystal highly suitable for radiation detection applications, owing to its effective luminescent response.

The above discussion indicates that several studies have been conducted on the properties of bulk alkaline earth metal halides with non-cubic or orthorhombic phases. However, their two-dimensional (2D) counterparts have been explored for possible applications in various fields. Compared to their 2D counterparts,  $\text{MX}_2$  materials exhibit more intriguing physical and chemical properties owing to quantum confinement effects and enhanced surface-to-volume ratios [26]. In addition to these 2D monolayer materials, the IIA-VIIA compounds often demonstrate increased flexibility, mechanical strength, and unique electronic properties that differ from their bulk counterparts when exfoliated into monolayer or few-layer structures [27]. For instance, these 2D materials can exhibit high carrier mobility, tunable bandgaps, and strong light-matter interactions, making them ideal candidates for next-generation electronics, photodetectors, and energy storage device applications [27].

The 2D doped- $\text{SrCl}_2$  monolayer induces half-metallicity and shows diluted magnetic semiconductor behavior with varying magnetism based on the specific dopant [28]. This tunable magnetism presents a promising potential for spintronic applications, where control over spin-polarized charge carriers is essential.  $\text{MgF}_2$  has become increasingly popular in laser device applications as an ideal antireflection coating and high-resistance laser damage material owing to its low refractive index and wide bandgap [29]. It is also a promising compound with excellent luminescent properties and a key material for long-distance optical fiber communication. Alkaline earth metal halide-based wide bandgap semiconductors are among other 2D materials that exhibit vacuum ultraviolet (VUV) light absorption [30]. They are also used in optical windows, lenses, and prisms [31]. These halides have recently been studied for their electronic and optical properties from bulk to monolayer for anti-reflection coating applications [32]. The anti-reflection properties of these materials were preserved from the bulk to monolayer materials.

$\text{SrI}_2$  is also one of the alkaline earth metal-based halides that exhibits a bandgap (4.50 eV) in its bulk noncubic crystalline form (e.g., orthorhombic crystal structure) [23]. The electronic properties of its 2D counterparts were examined [32]. However, its potential applications in optical devices and optoelectronics are yet to be explored. Another aspect of this material is the ability to tune its electronic properties. Various methods are used to tune the properties of these materials. Substitutional doping is a simple and feasible method for this purpose. This is the most widely used method in this field by the scientific community of computational materials science. Hence, the effects of doping on the properties of  $\text{SrI}_2$  monolayers were examined. Similar to other doped alkaline earth metal halides [24,25,33], we chose lanthanide series elements (Nd, Sm, and Ho) to examine the effect of doping on the electronic and optoelectronic properties of single-layer  $\text{SrI}_2$ .

Moreover, the  $\text{SrI}_2$  monolayer is expected to share many similarities with  $\text{SrCl}_2$  [32,34], making it a suitable material for investigation. The properties of  $\text{SrI}_2$  are expected to align closely with those of

$\text{SrCl}_2$ , leading to comparable behaviors in various applications. Therefore, studying  $\text{SrI}_2$  can provide valuable insight into its characteristics, which are analogous to those of  $\text{SrCl}_2$ . These limitations comprise the scope and motivation of this study. Therefore, we investigated a 2D single layer of  $\text{SrI}_2$  and determined its structural, dielectric, electronic, and optoelectronic properties using the density functional theory (DFT). The second section, computational and calculational details, provides a detailed discussion of the computational strategy adopted to perform electronic and optical calculations. The results obtained from the calculations in the second section are illustrated and explained in the third section (results and discussion). The main findings are summarized in the fourth section, conclusions section. In the following section, we explain the DFT strategy for determining the optoelectronic properties of pure and engineered  $\text{SrI}_2$  single-layer material.

## 2. Computational and calculation details

The physical properties of the pure and doped  $\text{SrI}_2$  monolayer material were determined by the DFT [35]. First, geometrical relaxation was performed with the generalized gradient approximation (GGA) [36] using the variable-cell optimization scheme of the OpenMX [37] DFT simulation package. It is based on a norm-conserving pseudopotentials [38]. The electron exchange-correlation potential was described by the GGA Perdew–Burke–Ernzerhof (GGA-PBE) method. In OpenMX DFT code, numerically optimized pseudoatomic orbitals were used as basis functions to expand the KohnSham wave functions [39]. The basis functions used were  $\text{Sr}10.0\text{-}s3p2d2$  and  $\text{I}7.0\text{-}s3p2d2f1$  for Sr and I, respectively. Here, the numerals attached to the elemental symbol indicate the cutoff radius used in Bohr. For instance, it is 10.0 and 7.0 Bohr for Sr and I atoms, respectively. Furthermore, the number attached to each atomic orbital represents the number of used optimized radial functions. For example, three, two, and two radial functions were used for the *s*, *p*, and *d* atomic orbitals of Sr and I atoms, respectively. Moreover, only one radial function is allocated to the *f* orbital of the I atom. A regular  $7 \times 7 \times 1$  *k*-point mesh with a cutoff energy of 240 Ry was used to solve the Poisson equation and numerical integration [40]. A variable cell optimization scheme was utilized for the geometry optimization. This scheme simultaneously optimizes the cell vectors and internal coordinates without any constraints. This geometry optimization scheme uses two combined methods: the rational function [41] and direct inversion iterative subspace [42] methods, with a Broyden–Fletcher–Goldfarb–Shanno [43–46] update for the approximate Hessian. The structure was optimized until the force on each atom was less than 0.0003 Hartree/Bohr. The convergence criterion of self-consistent energy was set to  $10^{-6}$  Hartree. The considered monolayer material was simulated using a  $3 \times 3 \times 1$  supercell with a total of 27 atoms. The unit cell contains three atoms (one Sr atom and two I atoms). This unit cell can be considered as two atomic layers on either side of the Sr atomic layer, forming an  $\text{AB}_2$ -type crystal structure with A = Sr and B = I atoms. A vacuum space larger than 10 Å is applied along the *z*-axis to ensure negligible interaction between the replicated images under the periodic boundary conditions. The electronic band dispersion calculations were performed for  $\Gamma$ -M-K- $\Gamma$  path in the first Brillouin zone (BZ). The DOS and optical calculations were performed using a regular *k*-point mesh of  $11 \times 11 \times 1$ .

In the OpenMX DFT code, the optical conductivity and dielectric functions were calculated using the KuboGreenwood (KG) formalism [47,48], which describes electromagnetic absorption in the one-electron approach. The dielectric function and conductivity tensors were computed using the Born approximation. These complex functions were calculated in linear response to an applied perturbing frequency-dependent oscillating electric field. A simplified form of the KG formula for calculating optical conductivity was derived by Moseley [49]. A material's response to the incident light can be examined

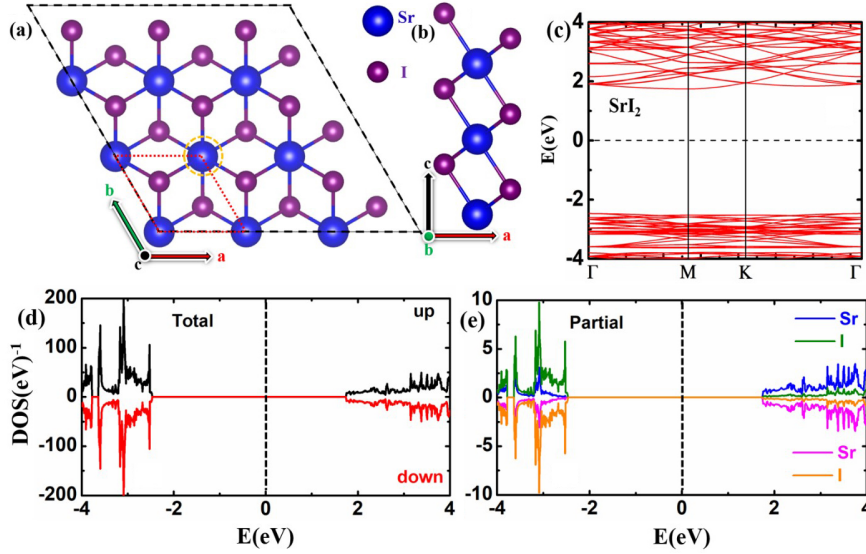


**Figure 1.** (a) Optimized crystal structure of  $\text{SrI}_2$  monolayer in the  $3 \times 3 \times 1$  supercell in the  $ab$ -plane (front view). The red dashed parallelogram is the representative of a unit cell. The substitutional doping of Nd, Sm, and Ho replaces a single Sr-atom surrounded by the orange-circled atomic site. (b) Side view of the crystal structure in (a), e.g., in the  $ac$ -plane. The Sr- and I-atoms are represented in the ball-stick model with blue and purple colors, respectively. (c) Band structure of the intrinsic  $\text{SrI}_2$  monolayer in the considered supercell. (d) and (e) are the total and partial DOS of the  $\text{SrI}_2$  monolayer and its constituent atoms, respectively.

by the dielectric function, represented as  $\epsilon(\omega) = \epsilon_1(\omega) + i\epsilon_2(\omega)$ . The contribution of intraband transitions to the  $\epsilon(\omega)$  is important only for materials with metallic features. In the current case, the material considered was a large bandgap material. Therefore, only the contribution from the interband electronic transitions is considered to calculate the imaginary part,  $\epsilon_2(\omega)$ , of the  $\epsilon(\omega)$ . It can be calculated by summing all possible direct electronic transitions from filled to vacant energy states. The mathematical expressions used to calculate the optical and dielectric functions in this study are as follows,

$$\epsilon_2(\omega) = \frac{Ve^2}{\hbar m^2 \omega^2} \int d^3k \sum_{n, n'} |\langle k, n | p | k, n' \rangle|^2 f(k, n) (1 - f(k, n')) \delta(E_k, n - E_{k, n'} - \hbar\omega). \quad (1)$$

In Eq. (1),  $\hbar\omega$  is the energy of the incident radiation,  $|k, n\rangle$  is the ket vector with an eigenvalue  $E_{k, n}$ ,  $p$  represents the momentum operator, and  $f(k, n)$  accounts for the Fermi distribution function. The real part,  $\epsilon_1(\omega)$ , of the dielectric function can be calculated by inserting the Eq. (1) into the Kramers-Kronig relation as follows,

$$\epsilon_1(\omega) = 1 + \frac{2}{\pi} P \int_0^\infty \frac{\epsilon_2(\omega') \omega'}{\omega'^2 - \omega^2 + i\eta} d\omega', \quad (2)$$

where  $P$  is the principal value of the integral. Other optical quantities, such as reflection ( $R$ ), transmission ( $T$ ), extinction coefficient ( $\kappa$ ), optical absorption ( $\alpha$ ), and refractive index ( $n$ ), can be derived from the real and imaginary parts of the dielectric function. They are expressed

as follows,

$$R(\omega) = \left| \frac{\sqrt{\epsilon(\omega)} - 1}{\sqrt{\epsilon(\omega)} + 1} \right|^2, \quad (3)$$

$$\kappa(\omega) = \frac{\left( \sqrt{\epsilon_1^2(\omega) + \epsilon_2^2(\omega)} - \epsilon_1(\omega) \right)^2}{\sqrt{2}}, \quad (4)$$

$$\alpha(\omega) = \sqrt{2}\omega \left[ \frac{\sqrt{\epsilon_1^2(\omega) + \epsilon_2^2(\omega)} - \epsilon_1(\omega)}{2} \right]^2, \quad (5)$$

$$n(\omega) = \left[ \frac{\sqrt{\epsilon_1^2(\omega) + \epsilon_2^2(\omega)} + \epsilon_1(\omega)}{2} \right]^2. \quad (6)$$

### 3. Results and discussions

First, we discuss the structural details of the optimized geometry. Following a discussion of the electronic properties, we explored the dielectric and optical responses of the materials under consideration. The details of the crystal structure are discussed below. A front view of the optimized crystal structure of the  $3 \times 3 \times 1$  supercell of the 2D  $\text{SrI}_2$  monolayer is shown in Fig. 1(a), whereas Fig. 1(b) shows a side view. This supercell contains 27 atoms (9-Sr and 18-I atoms). Each Sr atom is octahedrally bonded to six nearby I atoms. The two I atomic layers are in the AB stacking model on either side of the Sr atomic layer. It crystallizes in a trigonal structure (space group,  $\bar{p}3m1$ ), similar to transition metal dichalcogenides [50]. The optimized lattice constant ( $a = b$ ) is 4.87 Å. The calculated Sr-I and I-I distances,  $d_{\text{Sr-I}}$  and  $d_{\text{I-I}}$  in the optimized geometry of the intrinsic  $\text{SrI}_2$  monolayer are 3.33 and 3.52 Å, respectively. These values are comparable to those previously reported [32]. However, these structural parameters are slightly reduced in the Nd-, Sm-, and Ho-doped  $\text{SrI}_2$  monolayers. The decrease in these values was small for the Nd- and Sm-doped  $\text{SrI}_2$  monolayers and larger for the Ho-doped system. This decrease in the Sr-I and I-I distances may be attributed to their atomic radii. The atomic radii in



the periodic table exhibit a decreasing trend from left to right. Notably, the atomic radii of the Nd and Sm atoms are nearly the same approximately 2.29 Å, and it is 2.16 Å for Ho-atom. The atomic numbers of Nd, Sm, and Ho are 60, 62, and 67, respectively. Because Nd and Sm atoms have nearly the same atomic radii, the lattice parameters (e.g.,  $a = b$ ,  $d_{\text{Sr-I}}$ , and  $d_{\text{I-I}}$ ) are negligibly affected in the Nd- and Sm-doped  $\text{SrI}_2$  monolayers compared with the Ho-doped system. The atomic number and radius of the Sr atom are 38 and 2.49 Å, respectively. The lattice parameters of the Nd-, Sm-, and Ho-doped  $\text{SrI}_2$  monolayers changed significantly compared with those of the undoped monolayers. This is because of the large atomic radius difference between the dopant (Nd, Sm, and Ho) and host (Sr) atoms. This difference is greater for the Ho-doped system, hence, there is a larger deviation between the lattice parameters of the Ho-doped and pure  $\text{SrI}_2$  monolayers (Table I).

The thermodynamic stability of the structure was calculated using the cohesive energy method,

$$E_{\text{coh}} = \frac{E(\text{SrI}_2) - n(\text{Sr})E(\text{Sr}) - n(\text{I})E(\text{I})}{n(\text{Sr}) + n(\text{I})}, \quad (7)$$

where,  $E(\text{SrI}_2)$ ,  $E(\text{Sr})$ , and  $E(\text{I})$  are the total energies of the  $\text{SrI}_2$  monolayers, isolated Sr atom, and I atom, respectively.  $n(\text{Sr})$  and  $n(\text{I})$  are the total number of Sr and I atoms in the  $\text{SrI}_2$  monolayer. The obtained cohesive energy is approximately -3.39 eV. The negative value of the cohesive energy demonstrates good thermodynamic stability of the material under investigation. It was observed that the cohesive energies of all the doped  $\text{SrI}_2$  materials (e.g.,  $\text{SrI}_2\text{:Nd}$ ,  $\text{SrI}_2\text{:Sm}$ , and  $\text{SrI}_2\text{:Ho}$ ) were slightly less negative than that of the intrinsic structure, indicating the reduced thermodynamic stability of the doped  $\text{SrI}_2$  monolayer. Calculating the phonon dispersion is a way to examine the dynamical stability of the crystal geometry. A negative phonon frequency indicates an unstable crystal structure. However, the phonon dispersion of the  $\text{SrI}_2$  monolayer does not exhibit negative frequencies, indicating its structural stability [32]. Moreover, the I-atom containing alkaline earth metal halides are slightly less stable than their fluoride, chloride, and bromide counterparts [32]. In addition to these observations, it is also noticed that the  $\text{SrI}_2$  is less stable than  $\text{BaI}_2$  and more stable than  $\text{MgI}_2$  and  $\text{CaI}_2$  because its cohesive energy is more negative than those of  $\text{MgI}_2$  and  $\text{CaI}_2$  and less negative than that of  $\text{BaI}_2$  (Table I). The obtained structural parameters of the studied  $\text{SrI}_2$  monolayer agree with reported values and are compared with those of other alkaline earth metal iodides (Table I). The calculated structural details of the optimized geometry are reliable and sufficiently reasonable to further analyze the optoelectronic properties of the  $\text{SrI}_2$  monolayer. Therefore, we investigated the DOS and electronic band structure, followed by the dielectric and optical responses discussed below.

Next, we discuss electronic investigations (band structure and DOS) of the intrinsic  $\text{SrI}_2$  monolayer using DFT methods. The calculated band structure and DOS of the intrinsic  $\text{SrI}_2$  monolayer are shown in Figs. 1(c) and 1(e), respectively. In the band structure plot in Fig. 1(c), the energy of the selected system is shown on the ordinate (vertical axis). The electronic energy level of the highest occupied VB corresponds to the Fermi level. A large gap (approximately 4.21 eV) was

observed between the bottom of the CB (CBM) and the top of the VB (VBM). This indicates the wide bandgap semiconducting characteristics of the intrinsic  $\text{SrI}_2$  monolayer. The CBM is at the M-point, whereas the VBM is in between the  $\Gamma$ -M path. The locations of the CBM and VBM at different  $k$ -points indicate the indirect bandgap of the  $\text{SrI}_2$  monolayer. Moreover, the upper bands are nearly flat at the top of the VBM. The GGA-PBE approximation underestimates the bandgap [51]. However, the bandgap obtained in the current work is comparable to the value reported using the GGA-PBE scheme [32]. The observed electronic features of the  $\text{SrI}_2$  monolayer were further verified from the corresponding total and projected DOS, shown in Figs. 1(d) and 1(e), respectively. The total DOS (TDOS) revealed zero-energy states around the Fermi energy. Moreover, the spin-polarized DOS was symmetrically distributed concerning the states with zero DOS levels, indicating a spin-symmetric electronic band structure. This is also reflected in the overlapping energy levels in the band structure for up and down spin polarizations. The band structure was plotted for only one spin state, owing to the overlapping of the up and down spin states, as shown in Fig. 1(a). Deep insights into the TDOS can be drawn from the partial DOS (PDOS) from the constituent atoms (e.g., Sr and I atoms). The results are shown in Fig. 1(e). The top of the VB was mainly populated by the I atom, whereas the Sr atom contributed to the CB. The two octahedrally coordinated I atoms contributed equally to the TDOS. Therefore, the TDOS of the I atom is plotted for only one I atom. This equal contribution of electronic states to the TDOS from both I atoms can be further justified by the corresponding angular momentum projected DOS, as shown in Fig. 2. Figures 2(a) and 2(b) show the orbital projected DOS for both I atoms, indicating an equal contribution to the TDOS. Moreover, it can also be noticed that the I- $p_z$  orbital only populates the nearly flat portion at the top of the VBM. Its contribution decreases with increasing negative energy in the VB. The contribution to the TDOS increases for the I- $p_x$  and I- $p_y$  orbitals even at lower energies; the I- $s$  orbital has nearly zero contribution to the TDOS in the VB. The Sr atom contributed significantly to the TDOS around 4.0 eV. The CB is predominantly populated by Sr- $d$  orbitals [not shown in Fig. 2(c)]. The electronic states in the CB and DOS also had small admixture contributions from the  $s$ -,  $p$ -, and  $d$ -orbitals of the I atom. This feature is similar to that observed for  $\text{SrCl}_2$  [52]. Hence, it can be concluded that the VB and CB were predominantly populated by fulfilled I- $3p$  and empty Sr- $4d$  orbitals, respectively. This may be attributed to the electronic transfer of two electrons from the Sr- $5s^2$  orbital to the I- $3p^5$  orbital of each I atom, for example, one electron from the Sr- $5s^2$  orbital to the  $3p^5$  orbital of each I atom connected to the Sr atom, forming an  $\text{MX}_2$ -type configuration. This electronic charge transfer leads to the fulfilled I- $3p$  orbital of each I atom in the  $\text{SrI}_2$  monolayer. This charge transfer is similar to that occurring in a  $\text{SrCl}_2$  monolayer [28]. Moreover, it indicates the predominant ionic characteristic of the bonding between Sr and I atoms. Figure 2(d) shows that a large amount of charge accumulated around the I site compared to the Sr site, indicating ionic bonding between Sr and I atoms. However, this charge accumulation was small around Sr atoms. This shows that the covalent bonding character is quite small. This is equivalent to the fact that the I atoms gain charge from the Sr atom. Hence, the I atoms are electron-receiving and the Sr atom behaves like an electron looser. The net charge on each atom of the considered supercell of the  $\text{SrI}_2$  monolayer is shown in Fig. 2(e). This signifies that the Sr atom can donate 0.18 electrons in equal amounts of electrons to each connected I atom (e.g., each can receive 0.09 electrons from the Sr atom). Hence, the electronic band structure and DOS analysis show that  $\text{SrI}_2$  is a large bandgap semiconductor with distinct contributions to the TDOS from the Sr and I atoms. The conclusions drawn from the band structure and DOS of the pure  $\text{SrI}_2$  monolayer were similar to those of the  $\text{SrCl}_2$  monolayer [28]. These observations demonstrate the importance of investigating the electrical conductivity and optical characteristics of these materials, which are crucial for potential applications in optoelectronics and photovoltaics.

**Table I.** Obtained structural parameters of  $\text{SrI}_2$  monolayer. The structural details of other iodide-based alkaline earth metals have also been listed for comparison purposes.

| Structural parameters | This work      |                          |                          |                          | Other works [32] |                |                |                |
|-----------------------|----------------|--------------------------|--------------------------|--------------------------|------------------|----------------|----------------|----------------|
|                       | $\text{SrI}_2$ | $\text{SrI}_2\text{:Nd}$ | $\text{SrI}_2\text{:Sm}$ | $\text{SrI}_2\text{:Ho}$ | $\text{MgI}_2$   | $\text{CaI}_2$ | $\text{SrI}_2$ | $\text{BaI}_2$ |
| $a = b$ (Å)           | 4.87           | 4.81                     | 4.80                     | 4.78                     | 4.18             | 4.67           | 4.94           | 5.37           |
| $d_{\text{Sr-I}}$ (Å) | 3.33           | 3.31                     | 3.30                     | 3.21                     | 2.95             | 3.23           | 3.38           | 3.58           |
| $d_{\text{I-I}}$ (Å)  | 3.52           | 3.51                     | 3.50                     | 3.45                     | 3.38             | 3.57           | 3.60           | 3.59           |
| $E_{\text{coh}}$ (eV) | -3.39          | -3.35                    | -3.31                    | -3.26                    | -2.97            | -3.29          | -3.32          | -3.41          |

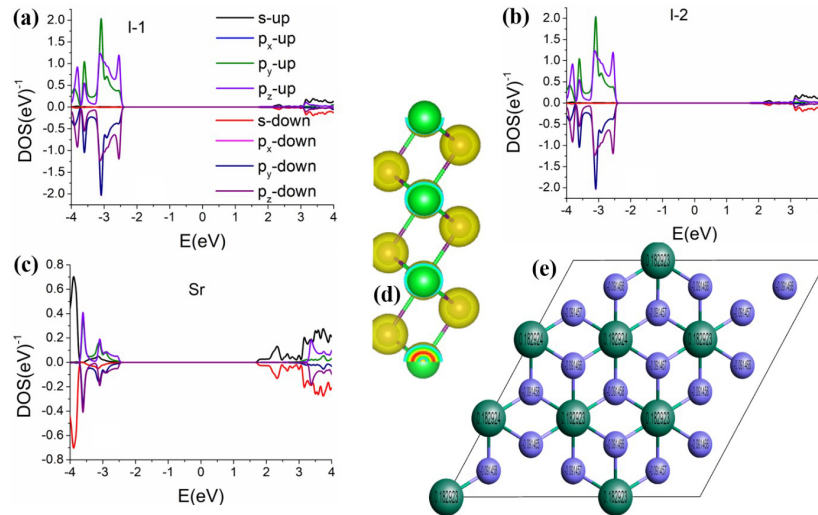


**Figure 2.** Spin-polarized orbital projected DOS of Sr- and I-atoms. (a) and (b) for two I-atoms (I1 and I2) and (c) for the Sr-atom. (d) Charge distribution in the  $\text{SrI}_2$  monolayer shows the ionic character of bonding between Sr and I-atoms. (e) Net charge on each atom in the compound. Sr- and I-atom are indicated by the green and blue colors, respectively.

Doping can alter the electronic properties of the  $\text{SrI}_2$  monolayers, as discussed above. Substitutional elemental doping is the most widely used method for computational research. The optoelectronic properties of bulk alkaline earth metal halides can be significantly altered by doping them with lanthanide series elements [21,24,25,33]. Motivated by these studies, we investigated the effects of doping on the properties of the  $\text{SrI}_2$  system. The substitutional doping method replaces the Sr-host atom of the  $\text{SrI}_2$  monolayer with one of the lanthanide series elements: Nd, Sm, or Ho. The doping effects of these elements on

the band structure and DOS are shown in Fig. 3. The spin degeneracy is partially lifted in the CB owing to the change in the chemical composition after substitutional doping. The doped system of the  $\text{SrI}_2$  monolayer is modeled using a  $3 \times 3 \times 1$  supercell, as shown in Fig. 1(a), by replacing one  $\text{Sr}^{2+}$  host ion with  $\text{Nd}^{2+}$ . This was equivalent to the doping percentage of 3.7 %. The percentage doping concentration was fixed for all the doped systems. The bandgap changes in the engineered system are not remarkable. The indirect bandgap features were preserved even after doping. The CBM and VBM are at the M-

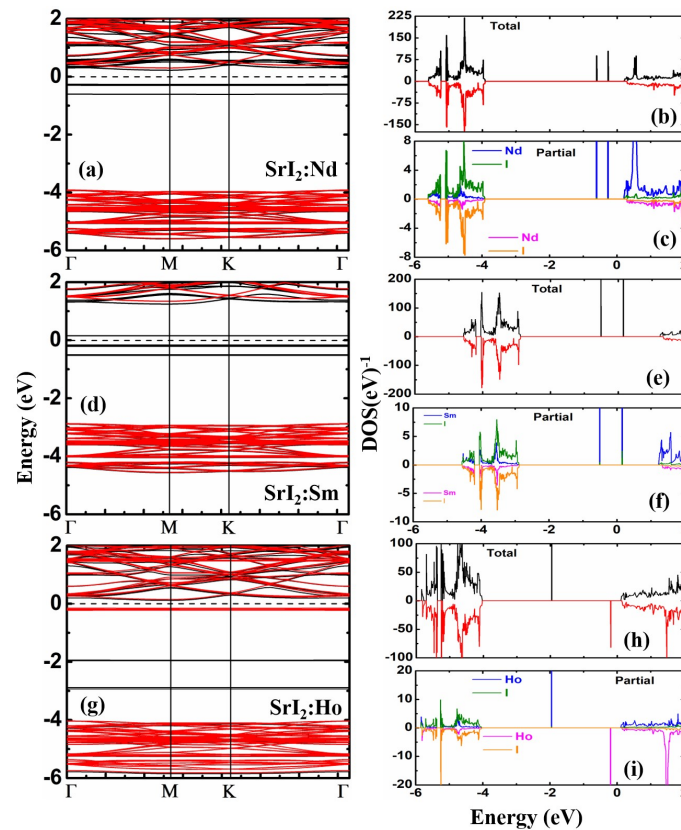


**Figure 3.** Calculated electronic band structures, TDOS, and PDOS of the  $\text{SrI}_2$  monolayer doped with (a–c) Nd, (d–f) Sm, and (g–i) Ho, respectively.

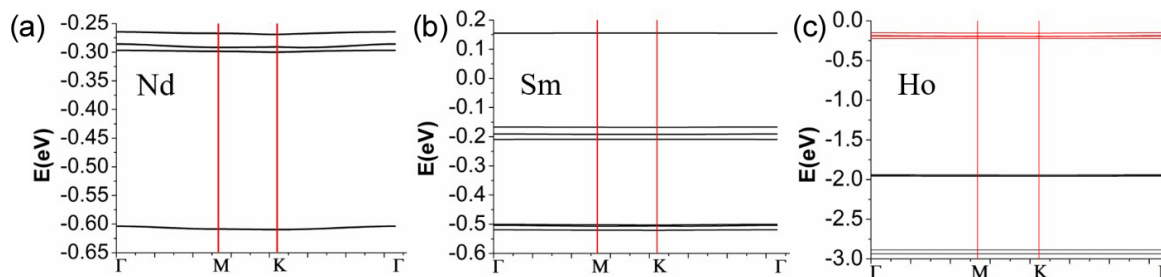


**Figure 4.** Zoomed-in part of the band structure around the Fermi level shows the contribution from the dopant atoms. The red vertical lines show the high symmetry points in the BZ. (a)  $\text{SrI}_2\text{:Nd}$ , (b)  $\text{SrI}_2\text{:Sm}$ , and (c)  $\text{SrI}_2\text{:Ho}$ .

and  $\Gamma$ -points of the first BZ for all doped cases; Figs. 3(a), 3(d), and 3(g), respectively. Moreover, the CB and VB bands shifted towards and away from the zero-energy level, respectively. Significant changes were observed in the band structures of the doped systems compared with their intrinsic forms.

More precisely, the electronic band structure changed significantly owing to the appearance of a nearly flat band around the zero-energy level. These flat bands were mainly attributed to the dopant element, for instance, Nd. The flat bands in the gap region are due to the  $f$ -atomic orbital of the dopant. The change in lattice geometry and orbital interference results in these flat bands in the gap region [53]. A low-energy plot of the band structure of all the doped systems is shown in Fig. 4. The flat bands in the VB of the Nd-doped system are between  $-0.25$  and  $-0.65$  eV. However, these are between  $0.17$  and  $-0.6$  eV and  $0.0$  and  $-3.0$  eV in the Sm- and Ho-doped  $\text{SrI}_2$  monolayer, respectively. The flat bands near the zero-energy level were due to the spin-down states of the Nd- and Sm-dopant atoms. However, the spin-up state contributes to the band structure of the Ho-doped system near the zero-energy level, and deep-lying flat bands (energy between  $-1.5$  and  $-3.0$  eV in the VB) are due to the spin-down states; see Fig. 3(g) and also refer to Fig. 4. In the current study, the appearance of flat bands in the electronic band structures around the zero-energy level in all doped systems was similar to that in the Tm-doped  $\text{SrCl}_2$  system [52]. Alternatively, it can be said that these flat bands, caused by the introduced impurity, represent the dispersion loss.

The corresponding DOS (total and partial) further confirmed these findings. The total and partial DOS of the Nd-, Sm-, and Ho-doped  $\text{SrI}_2$  monolayers are shown in Figs. 3(b), 3(c), 3(e), 3(f), 3(h), and 3(i), respectively. The TDOS in the VB is symmetrically distributed in the up- and down-spin states of the doped systems. However, it is clear from Fig. 3(b) that the DOS is not spin-symmetric around the zero-DOS level in the CB, confirming the breaking of the spin symmetry. Moreover, there were sharp peaks near zero energy in the VB, Fig. 3(b), of the Nd-doped  $\text{SrI}_2$  monolayer. The sharp peaks in the partial DOS of the Nd-doped  $\text{SrI}_2$  monolayer shown in Fig. 3(c) confirm the appearance of flat bands. There is a negligible overlap of the DOS from the nearest I atom to the DOS of the dopant atom.

Doping leads to the redistribution of electronic density in the system. The calculated net charges on each atom after the redistribution of the electronic densities are shown in Fig. 5. The blue atoms represent the dopant atoms in the ball stick model of the  $\text{SrI}_2$  monolayer. For instance, the net charges of the Nd, Sm, and Ho atoms in the host structure are approximately  $+0.82$ ,  $+0.41$ , and  $+0.29$  electrons, respectively. These net charges are larger than the net charge of the Sr atom at the dopant site. This may be attributed to the large difference between the atomic numbers of the dopant and host atoms. In contrast to the intrinsic  $\text{SrI}_2$  monolayer, where the charge distributions on each Sr and I atom are approximately the same [Fig. 2(e)], the net charge on each nearby I atom surrounding the dopant atom changes significantly. This effect was negligible for the I atoms away from the dopant site. The atomic density of Sr near the dopant site is also slightly affected. In the Nd-doped  $\text{SrI}_2$  monolayer, each of the nearest two I

atoms can receive approximately  $0.21$  electrons out of a net charge of  $+0.82$  electrons on the Nd-atom. The surplus electronic density on the Nd atom contributed to the DOS near the zero-energy level, as shown in Fig. 3(c). This gives rise to flat bands in the electronic band structure of the Nd-doped system, Fig. 4(a). A similar explanation applies to other dopants in the  $\text{SrI}_2$  monolayer, describing the occurrence of flat bands in their electronic band structures. Therefore, the net electronic density of the individual atoms further justifies the occurrence of flat bands in the electronic spectrum, resulting in significant changes in the electronic spectrum of the doped  $\text{SrI}_2$  monolayer compared to its intrinsic form. A recent study on the doped  $\text{SrCl}_2$  monolayers reported similar findings [54]. Hence, the current electronic investigations suggest that the engineered  $\text{SrI}_2$  monolayer material is a potential candidate for excellent luminescent properties, which can be further explored for use in advanced electronics, optoelectronics, energy materials, and scintillators.

The optical properties of a material can be derived from its electronic behavior. Intuitively, the optical properties of the  $\text{SrI}_2$  monolayer are modified by changes in its electronic properties due to the doping effect. Therefore, it is necessary to investigate the optical responses of the intrinsic and doped materials. It is also important to investigate the doping effects on the optical responses of pure materials. Therefore, we elaborated on the optical properties of undoped and doped  $\text{SrI}_2$  monolayers. This can be achieved by determining the frequency-dependent complex dielectric function. Therefore, in the discussion below, we illustrate and describe the results obtained from the DFT calculations. First, we discuss the dielectric function, optical absorption, and refractive index of intrinsic and doped  $\text{SrI}_2$  monolayers. The dielectric and optical quantities were determined for different light polarization directions, for example along three mutually perpendicular crystallographic directions. These are denoted as  $E||x$ ,  $y$ , and  $E||z$  for the direction of light polarization (perturbing field  $E$ ) along the  $x$ -,  $y$ -, and  $z$ -axes, respectively. The 2D  $\text{SrI}_2$  monolayer exhibited hexagonal symmetry. Hence, the in-plane optical response of the material (e.g., along the  $x$ - and  $y$ -crystallographic directions) was isotropic. Therefore, we plotted only the  $x$  components of the respective optical quantities in all illustrations. The dielectric functions

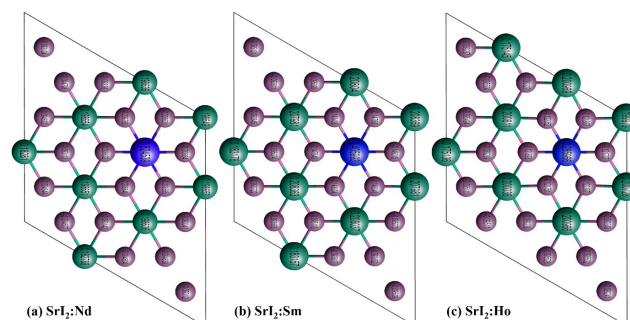


**Figure 5.** Net charge on each atom after redistribution of electronic density due to the doping effects. (a)  $\text{SrI}_2\text{:Nd}$ , (b)  $\text{SrI}_2\text{:Sm}$ , and (c)  $\text{SrI}_2\text{:Ho}$ .



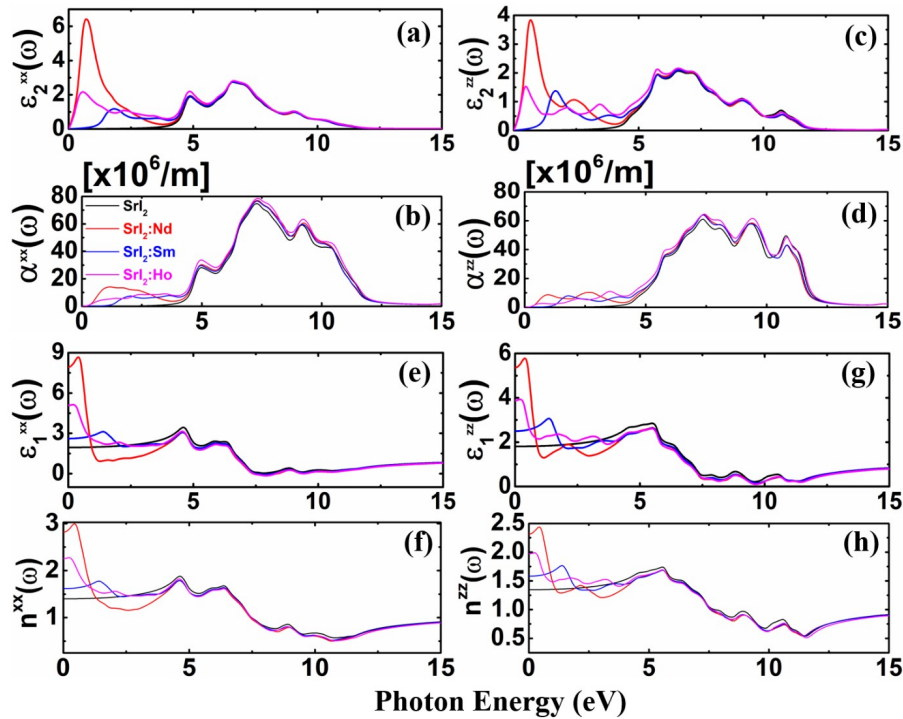


**Figure 6.** This figure illustrates the light polarization-dependent and frequency-dependent optical quantities. (a, b) and (c, d) the imaginary dielectric constant and optical absorption along the field polarization direction towards the x- and z-crystallographic axis, respectively. Similarly (e, f) and (g, h) are the real dielectric constant and refractive index along the x- and z-axis, respectively. Color consistency is followed in all illustrations, for example, the black, red, blue, and purple colors in all plots denote pure, Nd-, Sm-, and Ho-doped  $\text{SrI}_2$  monolayers, respectively.

(real and imaginary parts), optical absorptions, and refractive indices of the pure and lanthanides (Nd, Sm, and Ho) doped  $\text{SrI}_2$  monolayers are shown in Fig. 6. Color consistency is followed in all illustrations, for example, the black, red, blue, and purple colors in all plots denote pure, Nd-, Sm-, and Ho-doped  $\text{SrI}_2$  monolayers, respectively.

We first discuss the imaginary dielectric function ( $\epsilon_2$ ) along the x- and z-light polarization direction; Figs. 6(a) and 6(c). The dielectric function is a material-dependent property. It is shown for the energy ranging between 0.0 – 15.0 eV on the abscissa (on the x-axis). In the intrinsic case, both the components of  $\epsilon_2$  are nearly zero below 4.0 eV, indicating the material is transparent with minimum reflection to the light radiation. However, it increases with increasing photon energy and attains a first and second local maximum around 4.9 and 6.7 eV for the x-component. However, these are approximately 5.75 and 6.60 eV for the z-polarized component. These energies show the corresponding interband transitions in the electronic band structure, causing maximum light absorption in the UV region, indicating reduced transmission of light. The maximum light absorption can be observed in Figs. 6(b) and 6(d) along the x- and z-polarization directions, respectively. Both the components of  $\epsilon_2$  show a broad maximum peak spanning between 5.0 – 9.0 eV lying near the short-wavelength UV [ultraviolet-C (UVC) band] and the VUV region. The broad maximum of  $\epsilon_2$  is centered around the junction of the UVC and VUV regions. Moreover, it is also noticed that the  $\epsilon_2$  exhibits approximately the same behavior in the UVC and VUV regions for pure and doped systems, indicating that doping has no significant role. However, it has an important role in modifying the  $\epsilon_2$  in the energy region below 4.0 eV, a feature quite different from the pure material. The  $\epsilon_2$  has a finite value for each doped case in the low-frequency region. For example, the  $\epsilon_2$  in the  $\text{SrI}_2\text{:Nd}$  has a maximum of approximately 0.71 and 0.67 eV along the x- and z-polarization directions, respectively. This contribution to the  $\epsilon_2$  arises from the dopant Nd-atom. However, the Ho- and Sm-doped  $\text{SrI}_2$  monolayer exhibits the peak in the  $\epsilon_2$  around 0.48 (1.68) and 0.56 (1.84) eV along the z- and x-light po-

larization direction, respectively. These energy values span the short-wave infrared (IR) region to the visible region of the radiation spectrum, indicating that the material absorbs light. This feature in  $\epsilon_2$  of the pure material is absent. This signifies that the change in absorption that occurs in the doped materials is due to the impurity states. Most importantly, the response of the material to light radiation was different along the two light polarization directions. This shows the anisotropic character of the material to incident light radiation along the x- and z-crystallographic directions (e.g., the field polarization directions). This is a feature of uniaxial optical materials. This implies that the material exhibits uniaxial dielectric and optical anisotropy. Hence, similar to zirconia, it can be used to design ceramic-based antennae for space applications [55].

The real dielectric function ( $\epsilon_1$ ) represents the wave dispersion as it travels through the material medium. It also indicates the ability of the material to store the electrical energy and hence gives rise to the polarizability of the medium, e.g., the  $\epsilon_1$  indicates how much a material can be polarized under the perturbing electric field. It can also be described as the ability of a medium to permit a light field to travel through it. The  $\epsilon_1(\omega)$  is plotted in Figs. 6(e) and 6(g) against the energy of the perturbing field along two different polarization directions (x- and z-axis). In pure  $\text{SrI}_2$  monolayer, it is nearly constant in the short-wave IR to the visible region with a value of 1.96 and 1.79 in the x- and z-polarized direction, respectively. It slightly increases around 5.0 eV and then decreases with a further increase in the incident frequency, which attains nearly a unity value at higher frequencies. The real dielectric constant was higher in all doped cases than in the pure material in the far IR region. The static real dielectric constant is even more interesting, defined as the value of the  $\epsilon_1$  for zero-frequency, e.g., the  $\epsilon_1(\omega = 0)$ . It is nearly 7.90 (5.38), 5.10 (3.90), and 2.62 (2.53) for Nd-, Ho-, and Sm-doped  $\text{SrI}_2$  monolayer along x- (z-) polarization directions, respectively. It is clear from these values that Nd-doped  $\text{SrI}_2$  has the highest static dielectric constant along both directions compared to pure and the other dopants. This suggests that the incident

light penetrates the material over a large distance in the Nd-doped system, showing a greater dispersion of incident light. This also confirms that the material exhibits a high degree of in-plane polarization. Dispersion refers to the bending of light waves from their original paths. It measures the change in refractive index with wavelength. The calculated refractive indices of these materials for light polarized in the  $x$  and  $z$  directions are shown in Figs. 6(f) and 6(h), respectively. It shows a curve similar to that of a real dielectric function. This was nearly the same for higher frequencies around 15.0 eV in all materials. This confirms that doping does not affect the refractive index at higher energies. The refractive index changes significantly in the far IR to the visible region. The static refractive index ( $n$  for  $\omega = 0$ ) is the most important feature of a dielectric material. These are 1.40 (1.33, comparable to the water), 2.83 (2.30), 2.26 (1.97), and 1.63 (1.58) in the pure, Nd-, Ho-, and Sm-doped systems along the  $x$ - ( $z$ -) polarization direction, respectively. Doping significantly enhances the refractive index. It is maximum for Nd doping and minimum for Sm doping. The zero-frequency refractive index of the Sm-doped SrI<sub>2</sub> monolayer (1.63) along the  $x$ -axis was comparable to those of dense flint glass (1.65) and carbon disulfide (CS<sub>2</sub>, 1.628). The increased static refractive index supports the enhanced real static dielectric constants of the doped materials. The different behaviors of the wavelength-dependent refractive index along the  $x$ - and  $z$ -light polarization directions indicate the anisotropy of the medium. This is a property exhibited by a birefringent material. This was determined by the difference in the refractive indices along the  $x$ - and  $z$ -directions. This has also been observed in MoS<sub>2</sub> monolayers [56] and similar materials [30,57–59].

The light absorption depends on the imaginary dielectric function, e.g., the  $\epsilon_2$  of the material medium leads to light absorption. Hence, the absorption coefficients of these materials are expected to follow the curve of the imaginary dielectric function. The absorption coefficients of the pure, Nd-, Sm-, and Ho-doped SrI<sub>2</sub> monolayers along the  $x$ - and  $z$ -field polarization directions are illustrated in Figs. 6(b) and 6(d), respectively. The light absorption in the pure material is nearly zero for photon energies below 4.0 eV in both polarization directions, indicating the absence of light-matter interactions. This indicates that the material medium was transparent to these photon energies. A broad absorption peak between the photon energies 5.0 and 12.0 eV appears in the pure and doped SrI<sub>2</sub> monolayer. This again shows that impurity atoms do not affect the optical response in the UVC and VUV regions of the radiation spectrum. The impurity atoms significantly improve the optical response from the far IR to the visible regions. This can be further justified by the absorption peaks between 0.4 and 4.0 eV in the doped materials. Hence, the doped-SrI<sub>2</sub> monolayer can be used for visible light absorption, in addition to UVC and VUV light radiation. The absorption peaks indicate the extinction or attenuation of light radiation traversing the material medium. Notably, the absorption of light along the two polarization directions (i.e., the  $x$ - and  $z$ -directions) is different. This feature of the absorption coefficient again confirms their uniaxial optical anisotropic character, which we claimed when discussing the dielectric function.

The maximum absorption indicates a greater extinction of light. The light absorption spectrum of these materials is verified with the extinction coefficient,  $\kappa(\omega)$  (Fig. 7). The extinction coefficient implies the vanishing of falling light radiation on the material, which causes energy loss. This is equivalent to the absorption of radiation that reaches the medium. Alternatively, the extinction coefficient determines how quickly a medium absorbs incident light. The stronger the light absorption, the greater the light extinction coefficient. It also defines light wave attenuation in a material medium. The extinction coefficients of these materials are shown in Figs. 7(a) and 7(b) in the  $x$ - and  $z$ -polarization directions, respectively. These figures reveal that a broad light extinction region spans between 5.0 and 12.0 eV energy of the incident radiation in all materials, e.g., the extinction of light in these materials in this energy range is independent of the doping/impurity atom. However, the increased extinction below 5.0 eV

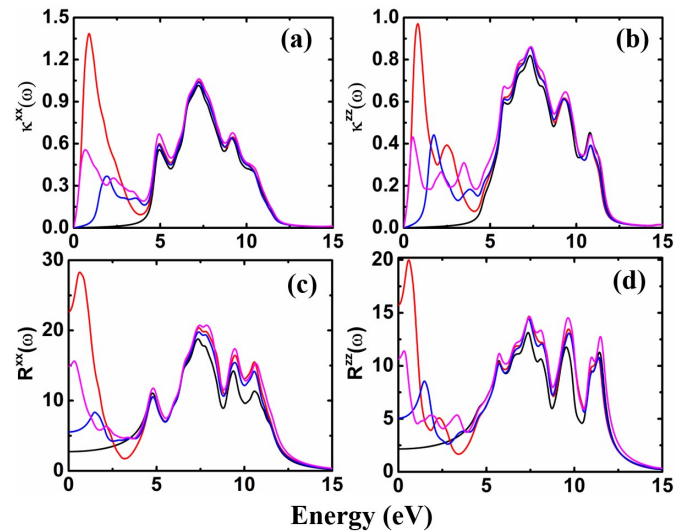


**Figure 7.** (a, b) Extinction coefficients and (c, d) the reflection coefficients in the undoped and engineered SrI<sub>2</sub> monolayer along two polarization directions, respectively. Color consistency is followed in all illustrations, for example, the black, red, blue, and purple colors in all plots denote pure, Nd-, Sm-, and Ho-doped SrI<sub>2</sub> monolayers, respectively.

of photon energy is only attributed to the impurity atoms. It was the highest for the Nd-doped SrI<sub>2</sub> monolayer (red-colored peak in the IR region), showing improved light absorption at low photon frequencies, as shown in Figs. 7(a) and 7(b). Similar peaks in the extinction coefficients were observed in the Sm- and Ho-doped SrI<sub>2</sub> monolayers. However, the peak intensity was slightly lower than that of the Nd-doped system, indicating lower light absorption. Notably, the extinction of incident light was greater along the  $x$ -polarization direction than in the  $z$ -direction. This may be because of the large distance traversed along the  $x$ -direction by the incident radiation within the material compared with the  $z$ -direction. The different extinction behaviors along the  $x$ - and  $z$ -directions indicate the uniaxial anisotropy of these material media. The extinction coefficient describes the backscattering of incident radiation induced by a reflecting medium [60]. Hence, it is equally important to determine the reflection of the incident light by the medium.

The reflection coefficients of the investigated materials are shown in Figs. 7(c) and 7(d) for the parallel and perpendicular polarization directions, respectively. The light reflection was less than 2.5 % in both polarization directions in the short-wave IR to the visible region for the pure material. This indicates the transparent characteristics of the medium at these incident wavelengths. This is verified by the corresponding transmission coefficient of the intrinsic SrI<sub>2</sub> monolayer, Fig. 8. The transmission coefficient was greater than 97 % for the pure SrI<sub>2</sub> monolayer along both polarization directions. This result agrees with the corresponding reflection spectrum, indicating that the medium is transparent to the respective radiation spectrum. Hence, the incident light did not interact significantly with the material. The reflection spectrum shows a broad peak between 5.0 and 12.0 eV, consistent with the corresponding transmission spectrum. This shows the mutual agreement between the reflection and transmission coefficients.

The decrease in the percentage transmission coefficient in this energy range indicates an increase in the reflection coefficient. All the doped materials showed similar behavior to the undoped material for wavelengths beyond visible light radiation. This confirms that substitutional doping (introduced impurity atoms) has no significant effect on the optical characteristics of the pure material for higher energies. However, they were found to have a pronounced effect on the optical response of pure SrI<sub>2</sub> at low energies. Both components in the doped material showed increased light reflection compared with the pure sys-



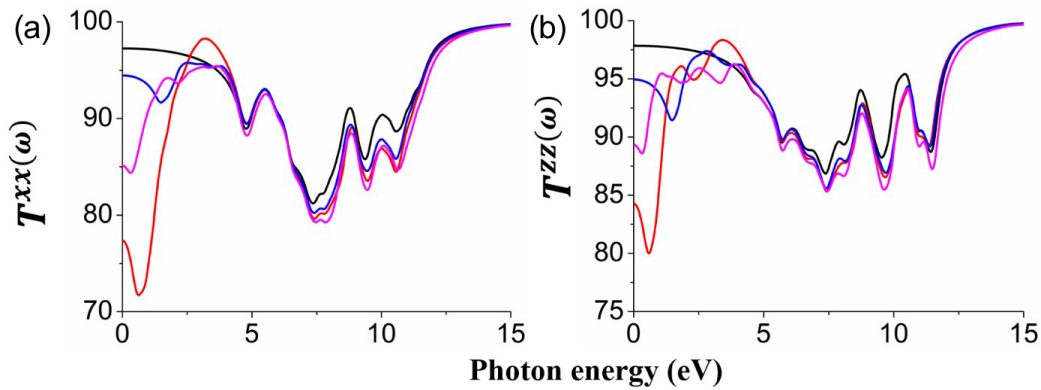


**Figure 8.** Change in the transmission coefficients of the doped and undoped materials along the (a)  $x$ - and (b)  $z$ -light polarization direction with varying incident photon energy. Color consistency is followed in all illustrations, for example, the black, red, blue, and purple colors in all plots denote pure, Nd-, Sm-, and Ho-doped  $\text{SrI}_2$  monolayers, respectively.

tem in the low-frequency region, Figs. 7(c) and 7(d). Hence, the corresponding transmission coefficient decreased, as shown in Fig. 8. For the doped cases, the reflection along both directions increases with the increased photon energy and reaches a maximum at 0.63, 0.34, and 1.5 eV in the Nd-, Ho-, and Sm-doping, respectively. The reflection suddenly decreased in the visible region with increasing energy and became nearly similar after 4.0 eV. The ups and downs in the reflection spectrum are the same as those in the corresponding transmission spectra. The most important is the static reflection (transmission) coefficient, defined as the value at the zero-photon frequency (e.g.,  $\omega \sim 0$ ). The static values of the reflection and transmission coefficients in the Nd-, Sm-, and Ho-doped materials along the  $x$  ( $z$ ) axis of the field polarization were approximately 23 and 77 (16 and 84), 6 and 94 (5 and 95), and 15 and 85 (11 and 89) %, respectively. These static values suggest that light reflection is less affected by the doping of the Sm atom in the  $\text{SrI}_2$  monolayer compared with the other dopants. The increased static reflection, and hence the decreased transmission, of light in the doped materials indicates the induced backscattering of the incident radiation due to the introduced impurity atoms, which behave like a more reflecting media [60]. The sharp decrease (increase) in the reflection (transmission) at low energies shows reduced backscattering of the incident photons from the impurity atom, signifying that the impurity atoms become less effective in modifying the optical response of the pure  $\text{SrI}_2$  material with increasing photon energy. Hence, it can be concluded that the introduced impurity atoms (dopants) play a noticeable role in tuning the optical response of the  $\text{SrI}_2$  monolayer. However, it is only applicable at low energies, below 4.0 eV.

The allowed interband optical transitions can be identified by the optical conductivity ( $\sigma$ ) response of a material. This is another optical parameter used to measure the optical response of a material

to an incident light field. This was used to determine the permitted optical interband transitions. It is also a complex quantity,  $\sigma(\omega) = \sigma_1(\omega) + i\sigma_2(\omega)$ . Its real part,  $\sigma_1(\omega)$ , corresponds to an in-phase response of the matter with the field. In contrast, the imaginary part,  $\sigma_2(\omega)$ , indicates the out-of-phase response to the light field. The real part indicates energy loss in the medium. Hence, it also indicates the absorption and extinction of light, representing the energy dissipation in the material. Furthermore, the imaginary optical conductivity is related to the ability of a material to store electrical energy, which gives rise to the nondissipative part of the conductivity response. This also indicates the inductive or capacitive characteristics of the material because they depend on the real dielectric function. The variation in  $\sigma_1$  along the  $x$ - and  $z$ -axis is elucidated in Figs. 9(a) and 9(b), respectively. It is seen that the  $\sigma_1$  along both the polarization directions are the same for pure and doped material above 4.0 eV, indicating the ineffectiveness of dopants in altering the light response. The  $\sigma_1$  has a broad maximum span from 5.0 to 12.0 eV. This broad maximum indicates the absorption of light for these energies and, hence, energy losses, thereby giving rise to energy dissipation. The  $\sigma_1$  is significantly affected by the impurity atoms only at low energies (below 4.0 eV). It has a noticeable finite value below 4.0 eV. This is due to impurity states-mediated optical transitions, for example, flat bands that appear in the gap region. However, it is approximately zero for pure material. The numerical value of  $\sigma_1$  is slightly higher along the  $x$ -direction than the  $z$ -direction. There is a sharp linear dependence of the  $\sigma_1$  in a narrow energy region around 5.0 eV. In addition, both components exhibited small but finite values of real optical conductivity, even at zero energy [61]. Therefore, the doped materials show a finite direct current optical conductivity, e.g.,  $\sigma_1(0)$ . It is the highest for the Nd-doped  $\text{SrI}_2$  monolayer. The variations in the imaginary optical conductivity

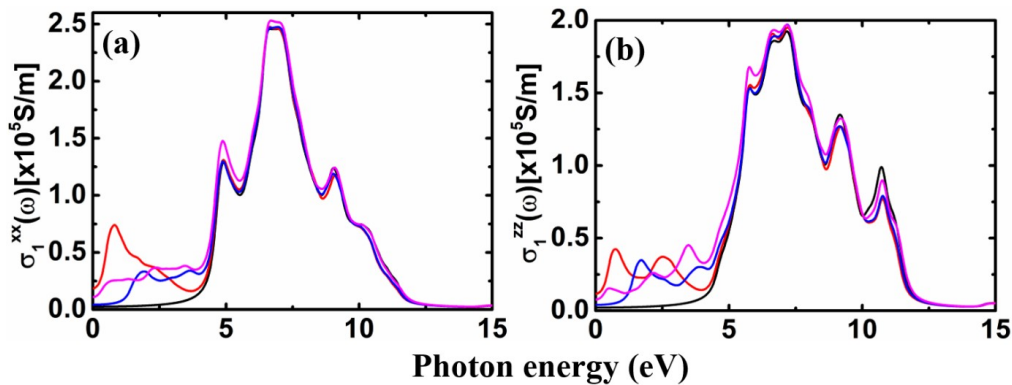


**Figure 9.** (a) and (b) show the real optical conductivities in pure and doped  $\text{SrI}_2$  monolayers along the  $x$ - and  $z$ -polarization directions, respectively. Color consistency is followed in all illustrations, for example, the black, red, blue, and purple colors in all plots denote pure, Nd-, Sm-, and Ho-doped  $\text{SrI}_2$  monolayers, respectively.

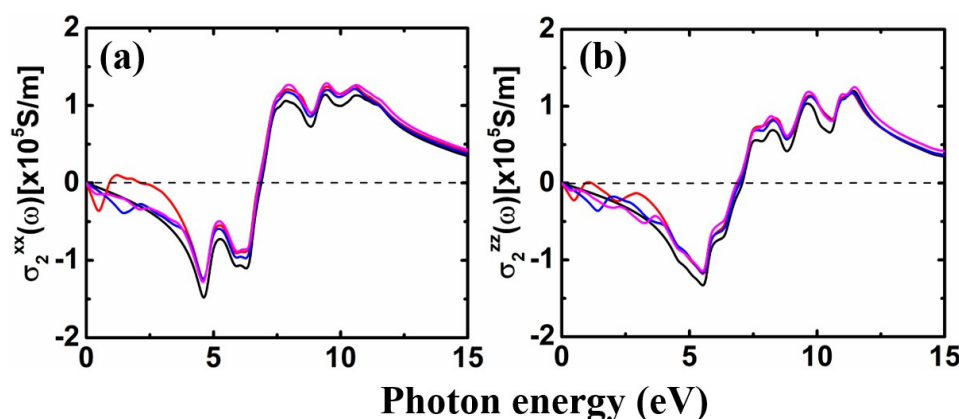


**Figure 10.** Imaginary part of the optical conductivity versus the incident field energy along the (a) x- and (b) z-polarization directions, respectively. Color consistency is followed in all illustrations, for example, the black, red, blue, and purple colors in all plots denote pure, Nd-, Sm-, and Ho-doped  $\text{SrI}_2$  monolayers, respectively.

with respect to energy are illustrated in Fig. 10. The overall trend of the imaginary optical conductivity decreased with an increase in photon frequency and remained negative between 0.0 and 7.0 eV. It changed sign (from negative to positive) with a further increase in energy. The change in sign indicates that the material is polarized in the opposite direction. The  $\sigma_1$  attains a maximum value near  $\sigma_2 \approx 0$ . Thereafter, the  $\sigma_1$  decreases and  $\sigma_2$  shows an increasing trend. For high incident photon energies both the  $\sigma_1$  and  $\sigma_2$  approach to a zero value.

#### 4. Conclusions

In this study, the electronic and optical responses of pure and lanthanide (Nd, Sm, and Ho) doped 2D  $\text{SrI}_2$  monolayer materials were investigated. First-principles DFT was used to perform all calculations in the GGA-PBE approximation. Electronic calculations indicate the wide bandgap insulating behavior of materials considered. The calculated electronic bandgap of the pure material was nearly 4.21 eV, which is comparable to previously reported values. The conclusions drawn from the band structure were corroborated by the total and partial DOS. The calculated electronic band structures and DOS agreed with each other. In addition, doping has no significant effect on the bandgap of the pure material. Hence, the doped materials preserve their wide bandgap semiconducting properties. However, impurity electronic states appear near the zero-energy level in the electronic band structure. These impurity states are attributable only to the dopant atoms (e.g., impurity atoms). The corresponding total and partial DOS also justify this result. The sharp peak in the DOS that occurs in all doped materials indicates the emergence of impurity states near the zero-energy level. The change in electronic properties is evident from the redistribution of electronic densities after doping.

The presence of impurity states changes the electronic transitions, resulting in a change in the linear optical response of the material. Therefore, we also investigated the frequency and polarization-dependent optical responses of the pure and doped materials. The doping significantly modified the dielectric and optical functions only at low energies, below 4.0 eV. However, the doping effect was not significant for photon energies higher than 5.0 eV. In addition to the UVC and VUV light absorption in these materials, visible light absorption was significantly enhanced in the Nd-doped  $\text{SrI}_2$  monolayer material, a feature absent in the pure material. Similarly, the frequency-dependent real static dielectric constant substantially enhances, resulting in an increased refractive index. The static refractive index of  $\text{SrI}_2\text{:Sm}$  ( $n = 1.63$ ) is comparable to that of carbon disulfide (1.628). A higher refractive index indicates an increased light reflection in the respective energy region. This suggests that the doped materials are less suitable for the anti-reflection coatings in their respective radiation spectra. However, pure  $\text{SrI}_2$  exhibited excellent anti-

reflection properties in the UVC and VUV regions, indicating its potential application in solar cells. Moreover, the optical response of the material is strongly anisotropic along the x- and z-axes, a feature of anisotropic optical materials. Therefore, these are uniaxially birefringent anisotropic optical materials. The obtained optical conductivity also showed significant changes in the short-wave IR to the visible region owing to the doping effect. These findings suggest that the materials under investigation have potential for nanoelectronic and optoelectronic device applications.

#### Acknowledgments

This research was supported by the National Research Foundation of Korea (NRF) grant funded by the Korean Government (MIST) (Grant No. 2022R1A2C1012996). PK thanks the Materials Simulation Research Center (MSRC), Manipal University, Jaipur, for providing a partial computational facility.

#### Conflict of interest

The authors declare no conflicts of interest.

#### ORCID

Vipin Kumar  
Pushpendra Kumar  
Jin Seog Gwag

<https://orcid.org/0000-0002-2211-2607>  
<https://orcid.org/0000-0002-4435-1430>  
<https://orcid.org/0000-0002-9699-5676>

#### References

- [1] J. Dai and Q. Feng, *Phys. Status Solidi B* 257, 1900726 (2020).
- [2] K. M. Fromm, *Dalton Trans.* 2006, 5103 (2006).
- [3] N. Kamanina, A. Toikka, Y. Barnash, P. Kuzhakov, and D. Kvashnin, *Materials* 15, 4780 (2022).
- [4] Y. Li, J. Zhang, H. Luo, D. Han, S. Wang, and G. Li, *Ceram. Int.* 50, 12968 (2024).
- [5] H.-M. Wang, L.-L. Yang, G.-R. Li, X. Zhu, H. Zhu, and Y.-T. Zhao, *J. Iron Steel Res. Int.* 20, 21 (2013).
- [6] S. Hull, S. T. Norberg, I. Ahmed, S. G. Eriksson, and C. E. Mohn, *J. Solid State Chem.* 184, 2925 (2011).
- [7] A. Aguado, A. Ayuela, J. M. López, and J. A. Alonso, *J. Phys. Soc. Jpn* 68, 2829 (1999).
- [8] G. Solt and J. Kollár, *Solid State Commun.* 16, 453 (1975).
- [9] C. Jouanin, J. P. Albert, and C. Gout, *J. Phys. France* 37, 595 (1976).

- [10] J. Chen, Z. Zhang, Y. Guo, and J. Robertson, *J. Appl. Phys.* 131, 215302 (2022).
- [11] P. Kumar and A. G. Vedeshwar, *AIP Conf. Proc.* 1675, 020013 (2015).
- [12] Y. Li, M. Wu, H. Chen, D. Xu, L. Qu, J. Zhang, R. Bai, and Y. Lan, *Front. Chem.* 7, 149 (2019).
- [13] W. Wang, R. Lemaire, A. Bensakhria, and D. Luart, *J. Anal. Appl. Pyrol.* 163, 105479 (2022).
- [14] F. Zhou, B. Sadigh, P. Erhart, and D. Åberg, *npj Comput. Mater.* 2 (2016).
- [15] K. M. Fromm, *Coord. Chem. Rev.* 408, 213193 (2020).
- [16] B. Kang, Q. Feng, C. Summers, C. M. Fang, R. Adhikari, and K. Biswas, *IEEE Trans. Nucl. Sci.* 64, 1817 (2017).
- [17] B. Kang, Q. Feng, and K. Biswas, *J. Phys. D: Appl. Phys.* 51 (2018).
- [18] N. J. Cherepy *et al.*, *Appl. Phys. Lett.* 92, 083508 (2008).
- [19] N. J. Cherepy *et al.*, *IEEE Trans. Nucl. Sci.* 56, 873 (2009).
- [20] H. Bärnighausen and N. Schulz, *Acta Cryst.* B25, 1104 (1969).
- [21] S. Lam, S. E. Swider, A. Datta, and S. Motakef, *IEEE Trans. Nucl. Sci.* 62, 3397 (2015).
- [22] S. E. Swider, S. Lam, and A. Datta, *IEEE Trans. Nucl. Sci.* 63, 2830 (2016).
- [23] D. J. Singh, *Appl. Phys. Lett.* 92, 201908 (2008).
- [24] A. S. Pushak, V. V. Vistovskyy, S. V. Myagkpta, T. M. Demkiv, O. T. Antonyak, J. R. Dacyuk, P. V. Savchyn, and A. S. Voloshinovskii, *Funct. Mater.* 17, 294 (2010).
- [25] D. Nakauchi, Y. Fujimoto, T. Kato, N. Kawaguchi, and T. Yanagida, *Crystals* 12, 517 (2022).
- [26] T. Dutta *et al.*, *Nano Mater. Sci.* 6, 1 (2024).
- [27] S. H. Lin and J. L. Kuo, *Phys. Chem. Chem. Phys.* 16, 20763 (2014).
- [28] V. V. On, R. Ponce-Pérez, C. V. Ha, J. Guerrero-Sanchez, and D. M. Hoat, *Phys. Scr.* 99, 065947 (2024).
- [29] M. Zhan, W. Gao, T. Tan, H. He, J. Shao, and Z. Fan, *Vacuum* 79, 90 (2005).
- [30] V. Kumar, R. K. Mishra, H. Jeon, P. Kumar, R. Ahuja, and J. S. Gwag, *J. Phys. Chem. Solids* 181, 111482 (2023).
- [31] J. Haber and M. Wojciechowska, *Catal. Lett.* 10, 271 (1991).
- [32] H. Alavi-Rad and S. B. Touski, *Phys. B* 676, 415650 (2024).
- [33] G. Sánchez-Sanz, L. Seijo, and Z. Barandiarán, *J. Chem. Phys.* 133, 114506 (2010).
- [34] C. Akyol, M. Baskurt, and H. Sahin, *J. Mater. Chem. C* 8, 12527 (2020).
- [35] W. Kohn and L. J. Sham, *Phys. Rev.* 140, A1133 (1965).
- [36] J. P. Perdew, K. Burke, and M. Ernzerhof, *Phys. Rev. Lett.* 77, 3865 (1996).
- [37] Welcome to OpenMX <http://www.openmx-square.org> (accessed Jan. 20, 2025).
- [38] I. Morrison, D. M. Bylander, and L. Kleinman, *Phys. Rev. B* 47, 6728 (1993).
- [39] T. Ozaki, *Phys. Rev. B* 67, 155108 (2003).
- [40] T. Ozaki and H. Kino, *Phys. Rev. B* 72, 045121 (2005).
- [41] A. Banerjee, N. Adams, J. Simons, and R. Shepard, *J. Phys. Chem.* 89, 52 (1985).
- [42] P. Császár and P. Pulay, *J. Mol. Struct.* 114, 31 (1984).
- [43] R. Fletcher, *Comput. J.* 13, 317 (1970).
- [44] D. Goldfarb, *Math. Comput.* 24, 23 (1970).
- [45] C. G. Broyden, *IMA J. Appl. Math.* 6, 76 (1970).
- [46] D. F. Shanno, *Math. Comput.* 24, 647 (1970).
- [47] R. Kubo, *J. Phys. Soc. Jpn* 12, 570 (1957).
- [48] D. A. Greenwood, *Proc. Phys. Soc.* 71, 585 (1958).
- [49] L. L. Moseley and T. Lukes, *Am. J. Phys.* 46, 676 (1978).
- [50] Q. Tang and D. E. Jiang, *Chem. Mater.* 27, 3743 (2015).
- [51] J. P. Perdew *et al.*, *Proc. Natl. Acad. Sci. USA* 114, 2801 (2017).
- [52] C.-G. Ma and M. G. Brik, *Phys. Status Solidi B* 250, 858 (2013).
- [53] L. Jin, N. Varnava, D. Ni, X. Gui, X. Xu, Y. Xu, B. A. Bernevig, and R. J. Cava, *Proc. Natl. Acad. Sci. USA* 120, e2218997120.
- [54] V. Kumar, G. K. Maurya, P. Kumar, and J. S. Gwag, *Comput. Condens. Matter* 41, e00971 (2024).
- [55] G. Mazingue, B. Byrne, M. Romier, and N. Capet, *2020 14th European Conference on Antennas and Propagation* (Copenhagen, Denmark, March 15-20, 2020).
- [56] I. Ben Amara, E. Ben Salem, and S. Jaziri, *J. Appl. Phys.* 120, 051707 (2016).
- [57] V. Kumar, R. K. Mishra, P. Kumar, L. G. Trung, and J. S. Gwag, *Photon. Nanostruct. Fundam. Appl.* 53, 101114 (2023).
- [58] V. Kumar, R. K. Mishra, G. J. Choi, J. W. Ryu, P. Kumar, and J. S. Gwag, *Luminescence* 38, 1368 (2023).
- [59] V. Kumar, H. Jeon, P. Kumar, and L. G. Trung, *J. Phys. Condens. Matter* 36, 115701 (2024).
- [60] C. Hauger, E. Baigar, and W. Zinth, *Opt. Commun.* 133, 72 (1997).
- [61] D. Santos-Cottin, Y. Klein, P. Werner, T. Miyake, L. de' Medici, A. Gauzzi, R. P. S. M. Lobo, and M. Casula, *Phys. Rev. Mater.* 2, 1 (2018).